



Contents lists available at ScienceDirect



Catalysis Today

journal homepage: www.elsevier.com/locate/cattod

Comparison of mesoporous SSZ-13 and SAPO-34 zeolite catalysts for the methanol-to-olefins reaction

Leilei Wu, Emiel J.M. Hensen*

Laboratory of Inorganic Materials Chemistry, Schuit Institute of Catalysis, Eindhoven University of Technology, PO Box 513, Eindhoven, 5600 MB The Netherlands

ARTICLE INFO

Article history:

Received 14 November 2013

Received in revised form 19 January 2014

Accepted 21 February 2014

Available online xxx

Keywords:

SAPO-34

SSZ-13

Methanol-to-olefins

Stability

Hierarchical zeolites

ABSTRACT

Several approaches to improve the catalytic performance of SSZ-13 and SAPO-34 for application as acid catalysts in the methanol-to-olefins (MTO) reaction were explored. Silylation of mesoporous SSZ-13 with a Si/Al ratio of 20 zeolite resulted in increased lifetime in the MTO reaction. Lowering the acidity of SSZ-13 by increasing the Si/Al ratio to 50 also increased the lifetime. The generation of additional mesoporosity in SSZ-13 with a Si/Al ratio of 50 by use of the organosilane octadecyl-(3-trimethoxysilylpropyl)-ammonium chloride (TPOAC) only resulted in a minor improvement of the lifetime. Attempts to synthesize mesoporous SSZ-13 at high Si/Al ratios by use of $(C_{22}H_{45}-N^+(CH_3)_2-C_4H_8-N^+(CH_3)_2-C_4H_9)Br_2$ ($C_{22-4}Br_2$) were unsuccessful, and instead ZSM-5 zeolite was obtained. Similarly, SAPO-34 could not be made hierarchical by using $C_{22-4}Br_2$ as a mesoporeogen. In this case, other AlPO-phases were obtained. Mesoporous SAPO-34 was synthesized by using TPOAC in the synthesis gel. The additional intracrystalline mesoporosity did not lower the deactivation rate of SAPO-34 as was earlier observed for SSZ-13. The total methanol conversion capacity per acid site for microporous and mesoporous SAPO-34 were however comparable. The lower acidity of the acid sites in SAPO-34 led to the complete utilization of the micropore space. This is to be contrasted to SSZ-13 zeolite, for which the increased rate of coke formation results in more extensive coking deactivation and underutilization of the micropore space.

© 2014 Elsevier B.V. All rights reserved.

1. Introduction

Light olefins are key chemical intermediates in the petrochemical industry, which are usually produced through non-catalytic cracking of petroleum feedstock. With the growing importance of alternative feedstocks, most notably cheap natural gas and coal, there is now growing interest in methanol as a chemical intermediate of the synthesis of olefins. The methanol-to-olefins (MTO) reaction has been intensively studied in the last decades [1–5]. HSAPo-34, a silicoaluminophosphate having the chabazite (CHA) pore topology is the commercial catalyst for the MTO reaction. The relatively low acidity of silicoaluminophosphates and the combination of large cavities with a diameter of 9.4 Å, which stabilize the methylated benzene catalytic intermediates, with small 8-ring pore openings (3.8 Å) result in high selectivity to light olefins, typically above 80%. An inherent drawback of HSAPo-34 as MTO catalyst, which is typical for methanol-to-hydrocarbons (MTH) conversion reactions in zeolites, is deactivation due to formation

of carbonaceous deposits. This requires intermittent regeneration of the catalyst in commercial operation. In China, the MTO process is being commercialized on a large scale as part of chemical plants that convert cheap coal via gasification to syngas followed by methanol manufacture, light olefin and polymer production [6]. Catalyst deactivation is dealt with by carrying out the MTO reaction in a fluidized bed with a regenerator in which part of the coke is burnt. This capital-intensive process would benefit from catalysts with a longer lifetime, because the size of the regeneration section could be reduced [7].

Recently, we have shown that the introduction of mesopores in HSSZ-13 crystals results in a substantial decrease of the negative effect of coke formation [8,9]. Further characterization of mesoporous and conventional HSSZ-13 showed that the better accessibility of the micropores results in more complete utilization of the micropore space for the MTO reaction. For the synthesis of mesoporous HSSZ-13, we were inspired by the approaches developed by the Ryoo group [10–12]. We employed a combination of a structure-directing agent (SDA) for CHA formation (trimethyladamantanammonium hydroxide) with a mesopore-generating template $C_{22}H_{45}-N^+(CH_3)_2-C_4H_8-N^+(CH_3)_2-C_4H_9)Br_2$, identified by predictive computational modeling. Our approach was recently

* Corresponding author. Tel.: +31 40 2475178; fax: +31 40 2455054.

E-mail address: e.j.m.hensen@tue.nl (E.J.M. Hensen).

shown to be more generally applicable for a wide range of zeolites [13]. When applied in the MTO reaction the presence of interconnected micro- and mesoporosity in HSSZ-13 substantially increases the total methanol conversion capacity [8,9]. The mesoporous HSSZ-13 zeolites exhibited a much greater lifetime than conventional HSSZ-13 in the MTO reaction at nearly similar light olefins yield. The increased lifetime is explained by better utilization of the micropore space. There are two competing effects of the introduction of mesoporosity: (i) increased accessibility of the micropore space and, accordingly, better utilization of the micropore space and (ii) increased rate of coke formation with increasing external surface (increasing mesopore volume). Due to the fast coke built-up in HSSZ-13, most of the coke forms in the external region of the zeolite. Maximum catalyst lifetime was obtained at a relatively low mesoporogen/SDA ratio.

In this work, we investigate further issues related to mesoporous CHA zeolites for the MTO reaction. First, we explore the possibility to further improve the catalytic performance of HSSZ-13 zeolite for the MTO reaction. Two approaches were followed, i.e. decreasing the Al content of the zeolite framework so as to lower the density of Brønsted acid sites and the rate of coking [14–16] and by silylating the acid groups at or close to the external zeolite surface. Second, we attempted to synthesize mesoporous HSAP-34 using the mesoporogen successfully employed for synthesis of mesoporous HSSZ-13, $C_{22}H_{45}-N^+(CH_3)_2-C_4H_8-N^+(CH_3)_2-C_4H_9)Br_2$. For comparison, we also used an amphiphilic organosilane, which has been shown to induce mesopores for AlPO-5 and AlPO-11 molecular sieves [12].

2. Experimental

2.1. Synthesis of materials

2.1.1. Template synthesis

$C_{22}H_{45}Br_2$: The surfactant ($C_{22}H_{45}-N^+(CH_3)_2-C_4H_8-N^+(CH_3)_2-C_4H_9)Br_2$ was synthesized following a published procedure [9]. First, 4.1 g (0.01 mol) 1-bromodocosane (Aldrich, 96%) was dissolved in 20 ml toluene and added dropwise into the 20 ml solution of 10.3 g (0.07 mol) N,N,N',N' -tetramethyl-1,4-butanediamine (Aldrich, 98%) in acetonitrile. The resulting solution was stirred for 3 h at room temperature and then mixed at 70 °C under reflux overnight. After cooling to room temperature, the solution was kept in a refrigerator at 4 °C for 1 h, filtered and washed with diethyl ether. The resulting solid was dried in a vacuum oven at room temperature. The product was ($C_{22}H_{45}-N^+(CH_3)_2-C_4H_8-N(CH_3)_2)Br$. Second, 3.7 g (0.007 mol) ($C_{22}H_{45}-N^+(CH_3)_2-C_4H_8-N(CH_3)_2)Br$ and 1.96 g (0.014 mol) 1-bromobutane (Aldrich, 98%) were dissolved in 110 ml of acetonitrile and then stirred in a reflux condenser at 70 °C overnight. Next, the solid product was quenched in refrigerator at 4 °C for 1 h, filtered, washed with diethyl ether and dried in a vacuum oven at room temperature. The resulting product was ($C_{22}H_{45}-N^+(CH_3)_2-C_4H_8-N^+(CH_3)_2-C_4H_9)Br_2$ (denoted as $C_{22}H_{45}Br_2$).

2.1.2. Synthesis of molecular sieves

SSZ-13(50): SSZ-13 was synthesized as described in literature [17]. An amount of 2 g of a 1 M NaOH solution, 4 g 0.5 M N,N,N -trimethyl-1-adamantanammonium hydroxide (TMAdOH, SACHEM, 25%) and 2 g deionized water were mixed together. 0.05 g aluminum hydroxide (Sigma Aldrich) was added to this solution under vigorous stirring. After 30 min, 0.24 g fumed silica (Sigma) was added. The resulting mixture was stirred at room temperature to obtain a homogeneous gel with the composition 20 TMAdOH: 10 Na_2O : Al_2O_3 : 100 SiO_2 : 4400 H_2O , which was then transferred into a Teflon-lined autoclave and kept in an oven at 160 °C for 4 days. The zeolite product was filtered, dried and calcined at 550 °C

for 10 h in static air. The proton form of the zeolite was obtained by triple ion exchange of the calcined zeolite with 1 M NH_4NO_3 at 70 °C for 2 h followed by calcination in static air at 550 °C for 4 h.

Meso-Zeo(50, $C_{22}H_{45}$): A zeolite with $Si/Al=50$ was synthesized in the same manner as SSZ-13 by combining $C_{22}H_{45}Br_2$ and TMAdOH as templates. The starting molar gel composition was 10 TMAdOH: 5 $C_{22}H_{45}Br_2$: 10 Na_2O : Al_2O_3 : 100 SiO_2 : 5000 H_2O , which was subjected to crystallization in a Teflon-lined stainless-steel autoclave at 160 °C for 6 days. After crystallization, the solid product was collected by filtration, washed with deionized water, and dried at 110 °C. The zeolites were finally calcined at 550 °C for 10 h in static air. The proton forms of the zeolites were obtained by triple ion exchange of the calcined form with 1 M NH_4NO_3 at 70 °C and calcination at 550 °C for 4 h in static air.

Meso-Zeo(50, TPOAC): A mesoporous zeolite was synthesized by using octadecyl-(3-trimethoxysilylpropyl)-ammonium chloride (TPOAC, ABCR) as a mesopore-directing organosilane surfactant. The gel molar composition was 4 TPOAC: 20 TMAdOH: 10 Na_2O : Al_2O_3 : 100 SiO_2 : 4400 H_2O . The mixture was stirred further at room temperature until a homogeneous gel was obtained. The resulting gel was transferred into a Teflon-lined stainless steel autoclave and kept at 160 °C for 6 days. Thereafter, the solid material was recovered by filtration. The catalysts were finally calcined at 550 °C for 10 h in static air. The proton form of the zeolite was obtained by triple ion exchange of the calcined form with 1 M NH_4NO_3 at 70 °C and calcination at 550 °C for 4 h in static air.

Meso-SSZ-13($C_{22}H_{45}$, 0.17)-sil: A mesoporous SSZ-13 with $Si/Al=20$ synthesized by $C_{22}H_{45}Br_2$ and TMAdOH as templates was treated with TEOS to deactivate the external surface [18]. To this purpose, 1 g dehydrated SSZ-13($C_{22}H_{45}$, 0.17) [8] in its proton form was suspended in a mixture of 50 ml *n*-hexane and 0.15 ml TEOS at 50 °C for 1 h. The silylated product was centrifuged, dried at 110 °C, and calcined in air in two steps: the temperature was increased to 120 °C at the rate of 5 ° min^{-1} for 2 h, and went to 550 °C at 0.2 ° min^{-1} for 4 h.

SAPO-34: SAPO-34 was synthesized according to a procedure described in a patent assigned to the Union Carbide Corporation [19]. Example 35 was followed in this work. To this end, aluminum isopropoxide, Ludox HS-30, orthophosphoric acid, and tetraethyl ammonium hydroxide (TEAOH) were used to obtain a homogeneous gel with the composition 2 TEAOH: 0.3 SiO_2 : Al_2O_3 : P_2O_5 : 50 H_2O . This gel was placed in a Teflon-lined autoclave and kept in oven at 200 °C for 5 days. Afterwards, the solid material was recovered by filtration.

Meso-SAPO: Mesoporous SAPO zeolites were synthesized by addition of octadecyl-(3-trimethoxysilylpropyl)-ammonium chloride (TPOAC, ABCR) as a mesopore-directing organosilane surfactant to the synthesis gel of SAPO-34. Two samples were prepared. In the first one, the silica source was stoichiometrically replaced by TPOAC so that a molar gel composition of 0.3 TPOAC: 2 TEAOH: Al_2O_3 : P_2O_5 : 50 H_2O was used. This sample is denoted by meso-SAPO(TPOAC, ∞), the infinity sign indicating the molar TPOAC/Si ratio. The other sample denoted by meso-SAPO(TPOAC, 0.04) was obtained by addition of a small amount of TPOAC to the synthesis of SAPO-34. The gel composition was 0.012 TPOAC: 2 TEAOH: 0.3 SiO_2 : Al_2O_3 : P_2O_5 : 50 H_2O .

Meso-SAPO($C_{22}H_{45}$, n): In this case, 50% and 100% of the TEAOH compound in the standard SAPO-34 synthesis was replaced by $C_{22}H_{45}Br_2$. The gel compositions were $C_{22}H_{45}Br_2$: 0.3 SiO_2 : Al_2O_3 : P_2O_5 : 50 H_2O : 2 $NH_3\cdot H_2O$ and TEAOH: 0.5 $C_{22}H_{45}Br_2$: 0.3 SiO_2 : Al_2O_3 : P_2O_5 : 50 H_2O : $NH_3\cdot H_2O$, respectively. The synthesis procedure for these two zeolites is similar to conventional SAPO-34. The zeolites are denoted as meso-SAPO($C_{22}H_{45}$, n), where n refers to the fraction of TEAOH replaced by $C_{22}H_{45}Br_2$ in the synthesis gel. All the materials were finally calcined at 550 °C for 5 h in static air before further use.

2.2. Physicochemical characterization

2.2.1. Basic characterization

X-ray diffraction patterns were recorded on a Bruker D4 Endeavor diffractometer using Cu K α radiation in the 2θ range of 5–60°. Elemental analyses were carried out by ICP-OES (Spectro Ciros CCD ICP optical emission spectrometer with axial plasma viewing). To extract the metals, the catalysts were dissolved in 1.5 mL of an acid mixture of HF/HNO₃/H₂O. Argon adsorption experiments were determined at 87.6 K on a Micromeritics ASAP 2020 instrument in static mode. The samples were outgassed at 400 °C for 8 h prior to the sorption measurements. The Langmuir adsorption isotherm model was used to determine the total surface area (S_L) in the p/p_0 range between 0.05 and 0.20. The mesopore volume (V_{meso}) and mesopore size distribution was calculated from the adsorption branch of the isotherm by the Barrett–Joyner–Halenda (BJH) method. The micropore volume (V_{micro}) was determined by the *t*-plot method (thickness range 0.34–0.40 nm).

2.2.2. Electron microscopy

Scanning electron microscopy (SEM) pictures were taken on a FEI Quanta 200F scanning electron microscope at an accelerating voltage of 3–5 kV. The catalysts were coated with gold prior to measurements. Transmission electron microscopy (TEM) pictures were taken on a FEI Tecnai 20 at 200 kV. The catalysts were suspended in ethanol and dispersed over a carbon coated holey Cu grid with a film prior to measurements.

2.2.3. Vibrational spectroscopy

FTIR spectra of CO adsorbed to the zeolite samples were recorded in the range of 4000–400 cm⁻¹ by a Bruker Vertex V70 v instrument. The spectra were acquired at a 2 cm⁻¹ resolution and averaged over 20 scans. The samples were prepared as thin self-supporting wafers of 5–10 mg cm⁻² and placed inside a controlled environment infrared transmission cell, capable of heating and cooling, gas dosing and evacuation. Prior to CO adsorption, the catalyst wafer was heated to 550 °C at a rate of 2 °C min⁻¹ in an oxygen atmosphere. Subsequently, the cell was outgassed at the final temperature until the residual pressure was below 5 × 10⁻⁵ mbar. The sample was then cooled to 80 K. CO was introduced into the sample cell via a sample loop (5 μ L) connected to a Valco six-port valve.

2.2.4. NMR spectroscopy

Nuclear Magnetic Resonance (NMR) spectra were recorded on a Bruker DMX-500 NMR spectrometer. For the ²⁷Al Magic Angle Spinning (MAS) NMR a standard Bruker MAS probehead was used with rotor diameter of 2.5 mm, at a spinning rate of 20 kHz. The ²⁷Al chemical shift is referenced to a saturated Al(NO₃)₃ solution.

2.3. Catalytic activity measurements

Catalytic activity measurements were carried out in a quartz tubular fixed-bed reactor. First, the zeolites were pressed, crushed and sieved in a particle size fraction between 250 and 500 μ m. Second, 50 mg of the shaped catalyst was placed in a quartz tube (inner diameter 4 mm) between two quartz-wool plugs. Prior to the reaction, the catalyst was activated at 550 °C in artificial air (30 mL min⁻¹) for 2 h. The methanol-to-olefins reaction was performed at 350 °C for SSZ-13 zeolites and 450 °C for SAPO zeolites. Methanol (Merck, 99%) was introduced to the reactor by flowing He through a saturator kept at -17 °C with the flow rate 30 mL min⁻¹. The WHSV was kept at 0.8 g g⁻¹ h⁻¹ and the effluent was analyzed online by gas chromatography (Compact GC Interscience equipped with TCD and FID detectors with RT-Q-Bond and Al₂O₃/KCl columns). The amount of coke deposited during the reaction was determined by thermogravimetric analysis (TGA)

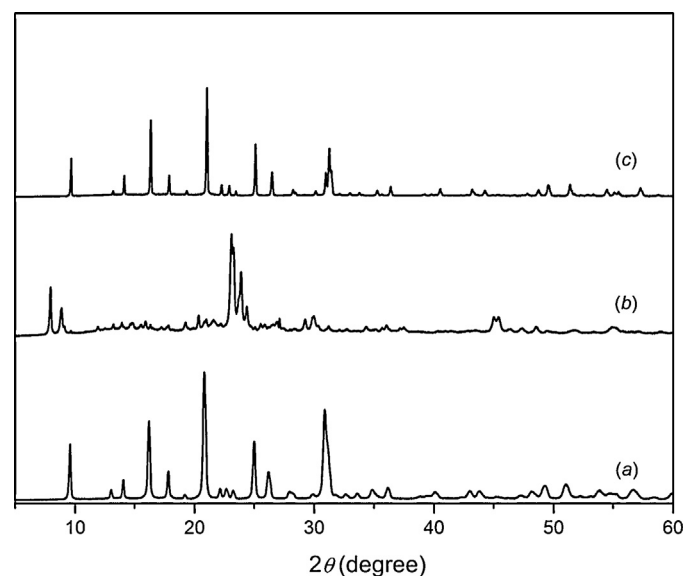


Fig. 1. XRD patterns of as-synthesized (a) SSZ-13(50), (b) meso-Zeo(50, C₂₂₋₄₋₄), and (c) meso-Zeo(50, TPOAC).

on TGA/DSC 1 STAR system of Mettler Toledo. The temperature was increased to 850 °C at a rate of 5 °C min⁻¹ under flowing air (50 mL min⁻¹).

3. Results and discussion

3.1. Synthesis and characterization

Fig. 1 shows the XRD patterns of the (aluminosilicate) zeolites synthesized at a gel Si/Al ratio of 50. The patterns of SSZ-13(50) and meso-Zeo(50, TPOAC) are consistent with predominant formation of crystalline zeolite with the CHA topology. The pattern of meso-Zeo(50, C₂₂₋₄₋₄) is that of MFI zeolite. The XRD patterns of the calcined zeolites (not shown) are very similar to those of the as-synthesized zeolites. SEM images show relatively large pseudo-cubic crystals for the bulk SSZ-13 zeolite (**Fig. 2**). These crystals are more rounded than the crystals synthesized at a Si/Al ratio of 20 [8]. TEM images of meso-Zeo(50, C₂₂₋₄₋₄) evidence that the crystalline domains of the ZSM-5 zeolite are relatively small, suggesting that the mesoporogen limited the crystal growth also in this case, although no CHA zeolite had formed. The zeolite prepared with TPOAC has the same morphology as a sample prepared at a Si/Al ratio of 20 [8], however, with less well-defined cubic crystals (**Fig. 2c**). This material is well-crystallized and made up from many small crystals.

Fig. 3 shows Ar physisorption isotherms and BJH pore size distributions of the calcined zeolites. The textural properties derived thereof are summarized in **Table 1**. The isotherm of SSZ-13(50) is type I, which is characteristic for microporous materials. The isotherms of the two zeolites synthesized with mesopore-directing agents have typical type IV isotherms, representative of mesoporous materials. All three materials have high Langmuir surface areas. The total pore volume of meso-Zeo(50, C₂₂₋₄₋₄) is substantially lower than for the other two zeolites, consistent with dominant formation of ZSM-5 zeolite, which usually exhibits pore volumes around 0.15 cm³ g⁻¹. The physisorption isotherm signifies that uniform mesopores have formed in this material. The use of TPOAC in SSZ-13 synthesis led to a relatively small increase of the mesopore volume as compared to the use of C₂₂₋₄₋₄Br₂ for SSZ-13 with a Si/Al ratio of 20 [8,9]. The pore size distribution curves in **Fig. 3** do not provide evidence for formation of ordered mesoporosity.

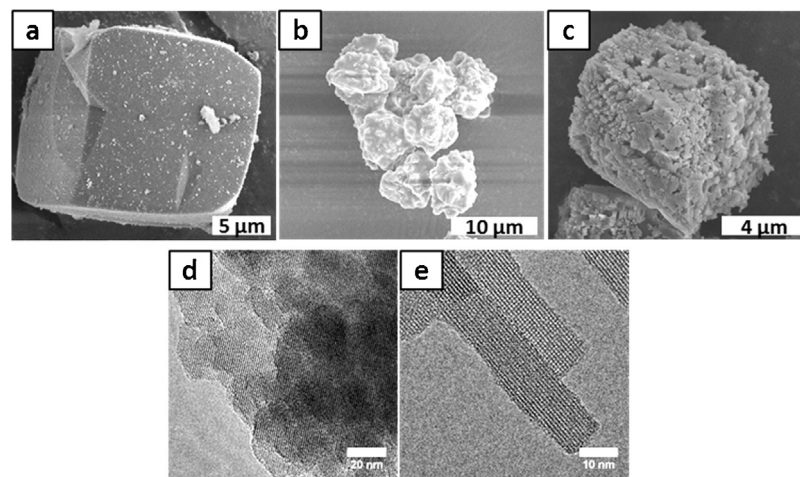


Fig. 2. SEM (a–c) and TEM (d and e) images of (a) SSZ-13(50), (b and d) meso-Zeo(50, C₂₂₋₄₋₄), and (c and e) meso-Zeo(50, TPOAC).

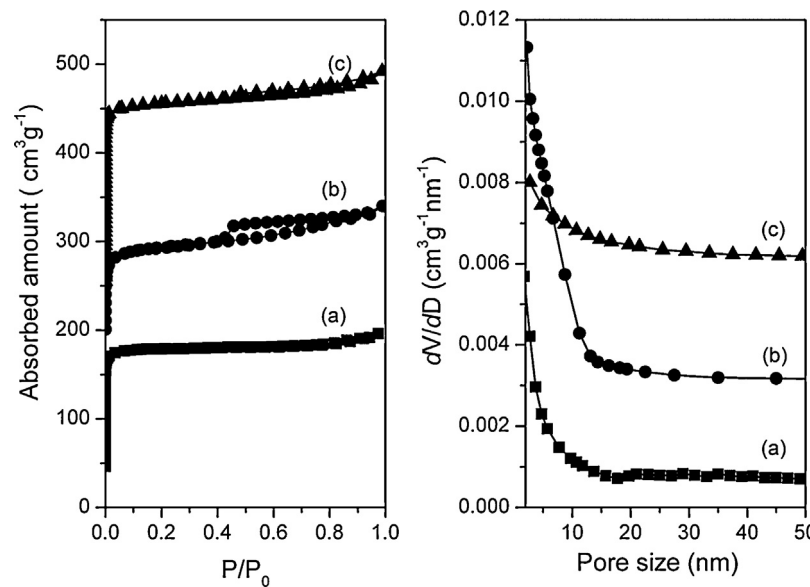


Fig. 3. Ar physisorption (left) and pore size distribution (right) of (a) SSZ-13(50), (b) meso-Zeo(50, C₂₂₋₄₋₄), and (c) meso-Zeo(50, TPOAC). The isotherms were vertically offset by equal intervals of 150 cm³ g⁻¹. The pore size distribution was calculated via BJH algorithm using the adsorption branch and vertically offset by equal intervals of 0.003 cm³ g⁻¹ nm⁻¹.

²⁷Al MAS NMR spectra of these three zeolites (not shown) are dominated by a feature around 59 ppm, which is characteristic for tetrahedrally coordinated Al atoms in the zeolite framework. A small feature around 0 ppm is assigned to octahedral Al species. Deconvolution of ²⁷Al MAS NMR spectra shows that more than 90%

of the Al species is built into the zeolite framework for all three samples.

Fig. 4 shows XRD patterns for SAPO-34, meso-SAPO(TPOAC) and meso-SAPO(C₂₂₋₄₋₄). The meso-SAPO(TPOAC) material has the CHA structure similar to SSZ-13 and SAPO-34. Compared to the

Table 1

Textural properties of the calcined SSZ-13 and meso-SSZ-13 materials determined by Ar physisorption.

Sample	Si/Al ratio ^a	S _L ^b (m ² g ⁻¹)	V _{tot} ^c (cm ³ g ⁻¹)	V _{meso} ^d (cm ³ g ⁻¹)	V _{micro} ^e (cm ³ g ⁻¹)
SSZ-13(50)	54	599	0.22	0.01	0.20
meso-Zeo(50, TPOAC)	61	792	0.31	0.04	0.22
meso-Zeo(50, C ₂₂₋₄₋₄) ^f	51	558	0.24	0.06	0.14
SAPO-34	–	735	0.30	0.03	0.22
meso-SAPO(TPOAC, 0.04)	–	778	0.36	0.11	0.21
meso-SAPO(C ₂₂₋₄₋₄ , 100)	–	247	0.55	0.51	0

^a Si/Al ratio of aluminosilicate zeolites determined by ICP elemental analysis.

^b S_L is the Langmuir surface area obtained in the relative pressure range (p/p_0) of 0.05–0.20.

^c V_{tot} is the total pore volume at $p/p_0 = 0.97$.

^d V_{meso} is the mesopore volume calculated from BJH method.

^e V_{micro} is the micropore volume calculated from t-plot method.

^f Predominantly ZSM-5.

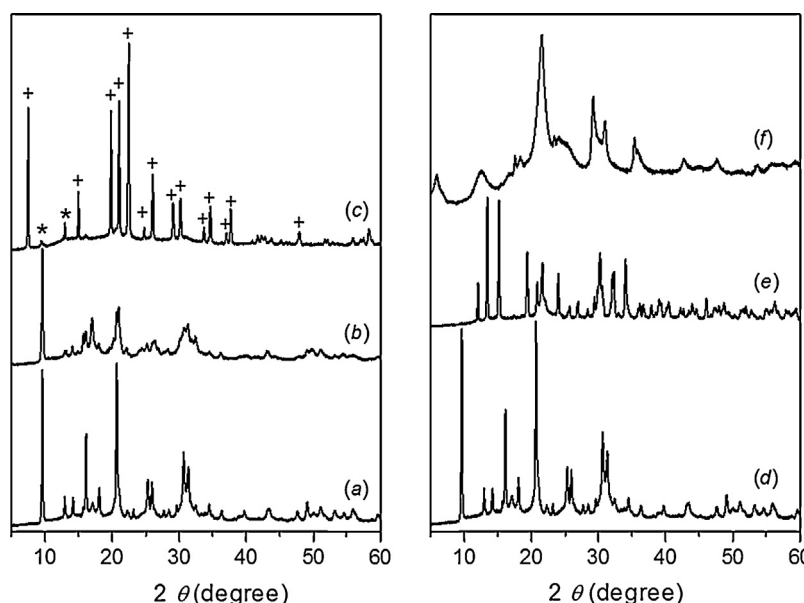


Fig. 4. XRD patterns of as-synthesized (a) SAPO-34, (b) meso-SAPO(TPOAC, 0.04), (c) meso-SAPO(TPOAC, ∞), (d) SAPO-34, (e) meso-SAPO(C_{22-4-4} , 50), and (f) meso-SAPO(C_{22-4-4} , 100) (* and + indicate reflections of CHA and AFI phases).

SAPO-34 reference, the reflections for meso-SAPO(TPOAC, 0.04) are, however, substantially lower and broader, which is indicative of the smaller size of the crystalline domains for this mesoporous material. When all Si of the Ludox HS-30 silica source in the synthesis gel has been replaced by TPOAC, AlPO-5 (AFI topology) was obtained with only a small amount of SAPO-34 (Fig. 4c). The AlPO-5 structure contains one-dimensional 12-membered ring channels. Similar to the successful synthesis of mesoporous SSZ-13 [8], we also attempted to use the diquaternary ammonium-type surfactant $C_{22-4-4}Br_2$ to obtain mesoporous SAPO-34. Two different synthesis gel compositions were used in which either half or all of the TEAOH in a typical gel for SAPO-34 synthesis was replaced by $C_{22-4-4}Br_2$ (equivalent amount of N atoms). The XRD patterns of meso-SAPO(C_{22-4-4} , 50) and meso-SAPO(C_{22-4-4} , 100) are shown in Fig. 4e and 4f, respectively. In neither case, SAPO-34 was formed. Meso-SAPO(C_{22-4-4} , 50) turned out to have the AlPO-15 structure [20,21], whilst the structure of the other material could not be matched with patterns from known databases.

Electron microscopy shows that SAPO-34 consists of small particles intergrown into larger agglomerates (Fig. 5). The crystals of the mesoporous SAPO-34, meso-SAPO(TPOAC, 0.04), are slightly smaller than those of SAPO-34. The AlPO-5 sample consists of large intergrown particles. The SEM image of AlPO-15 (meso-SAPO(C_{22-4-4} , 50)) shows large crystals with a square prism morphology without any sign of mesoporosity. The scanning and transmission electron micrographs for meso-SAPO(C_{22-4-4} , 100) are very different and show the formation of agglomerates of a layered material. Its layered nature is consistent with the presence of a low-angle diffraction peak in Fig. 4f. The significant background in this XRD pattern around 23° and the observation of globular particles by TEM (Fig. 2i) indicates that a significant amount of amorphous silica was also present. All this suggests that crystallization of this novel material is far from complete.

The Ar physisorption isotherms of SAPO-34, meso-SAPO(TPOAC, 0.04) and meso-SAPO(C_{22-4-4} , 100) are shown in Fig. 6 and the textural properties are listed in Table 1. The isotherm of SAPO-34 is of type I. The isotherm of meso-SAPO(TPOAC, 0.04) is a combination of type I and IV, which is characteristic of porous materials containing micro- as well as mesopores. Meso-SAPO(TPOAC, 0.04) has a similar surface area and micropore volume as SAPO-34, but its mesopore

volume is substantially higher ($0.11\text{ cm}^3\text{ g}^{-1}$ vs. $0.03\text{ cm}^3\text{ g}^{-1}$ for SAPO-34). It can be seen that the micropore volumes of SAPO-34 and meso-SAPO(TPOAC, 0.04) are very similar to the micropore volume of SSZ-13(50). The textural properties of meso-SAPO(C_{22-4-4} , 100) show that this layered material does not contain micropores.

Summarizing, we have found that the use of TPOAC results in a small amount of mesopores in high-silica ($\text{Si}/\text{Al} = 50$) SSZ-13. Attempts to employ $C_{22-4-4}Br_2$ as mesoporogen to synthesize hierarchical SSZ-13 at this relatively high Si/Al ratio were unsuccessful. Instead, the more stable ZSM-5 zeolite formed. Similar observations were made when these strategies were employed to SAPO-34 synthesis. Addition of small amounts of TPOAC to the synthesis gel of SAPO-34 led to generation of significant mesoporosity in SAPO-34. An increase of the TPOAC content led to nearly exclusive formation of AlPO-5 instead of SAPO-34. The use of $C_{22-4-4}Br_2$ during SAPO-34 synthesis resulted in formation of other phases than SAPO-34.

Before discussing the catalytic activity of some of these materials in the MTO reaction, we will first compare the acidity of SAPO-34 and meso-SAPO(TPOAC, 0.04). Fig. 7 displays the FTIR spectra of increasing doses of CO adsorbed on calcined SAPO-34 and meso-SAPO(TPOAC, 0.04). The high-frequency (HF) band at 3630 cm^{-1} and the low-frequency (LF) band at 3600 cm^{-1} are assigned to Brønsted acid sites. The intensities of these bands for meso-SAPO(TPOAC, 0.04) are lower than those for SAPO-34, which indicates that the mesoporous zeolite has a smaller number of Brønsted acid sites. Upon CO adsorption, the bands due to Brønsted acid sites shift to 3360 cm^{-1} . The equal red-shift of the hydroxyl frequency, $\Delta\nu(\text{OH}) = -270\text{ cm}^{-1}$, demonstrates that the strength of the acid sites in these molecular sieves is very similar. The shift is smaller than typically observed for the aluminosilicate zeolites, which are indeed usually considered to be stronger Brønsted acids [22,23]. Upon increasing the CO pressure, the HF band erodes faster than the LF band, which points to stronger acidity or better accessibility of the former hydroxyl groups. The spectra representing the CO stretching are also shown. The band at 2171 cm^{-1} appearing upon CO exposure is ascribed to CO adsorbed on Brønsted acid sites. Consistent with the view put forward by Almutairi et al., the polarization of the CO bond is not an adequate indicator of Brønsted acidity, as the blue shift of perturbed CO to 2171 cm^{-1} is similar to that for the stronger acidic HZSM-5 zeolite [14,24].

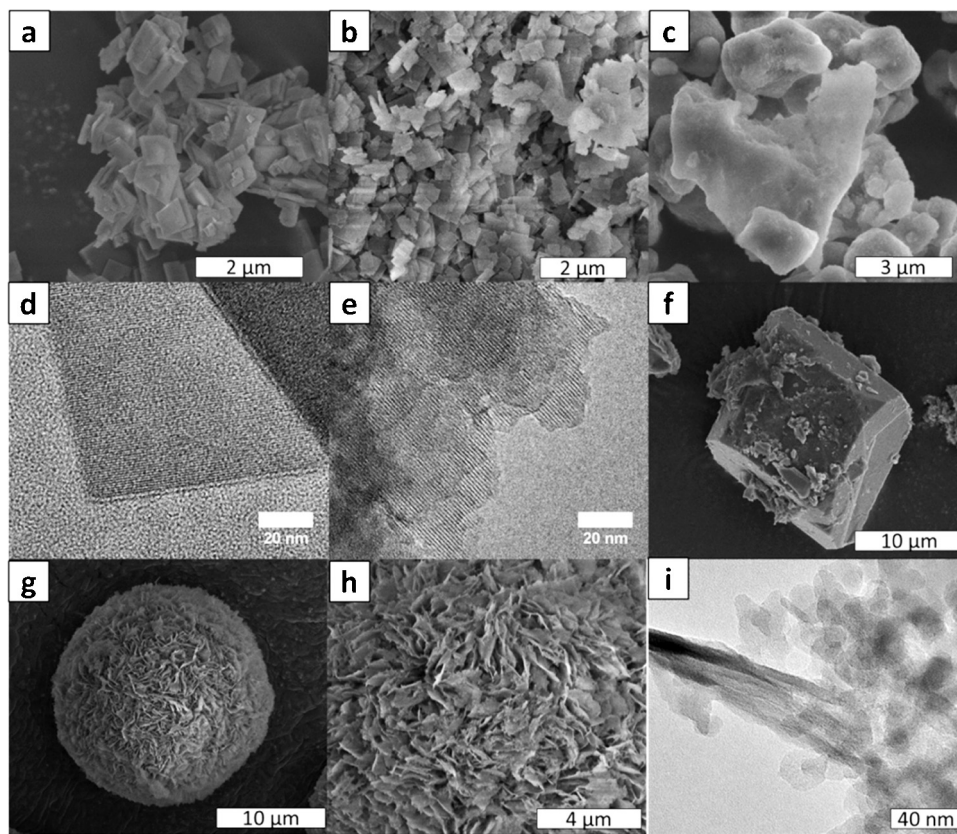


Fig. 5. Electron microscopy images of (a) conventional SAPO-34, (b and d) meso-SAPO(TPOAC, 0.04), (c and e) meso-SAPO(TPOAC, ∞), (f) meso-SAPO(C_{22-4-4} , 50), (g-i) meso-SAPO(C_{22-4-4} , 100).

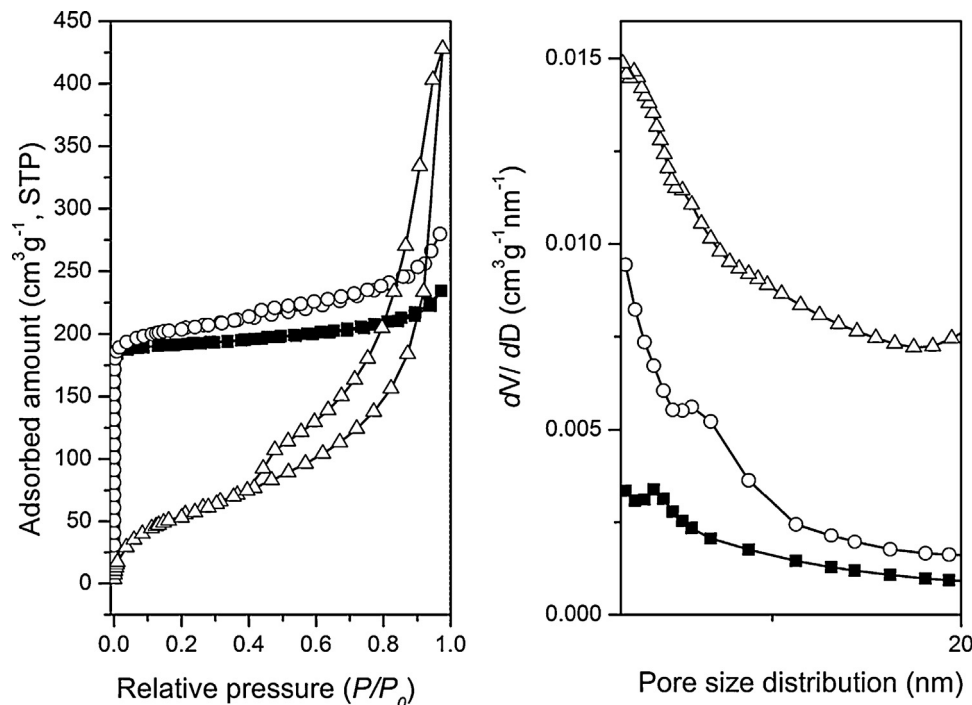


Fig. 6. Ar physisorption (left) and PSD (right) of (■) SAPO-34, (○) meso-SAPO(TPOAC, 0.04) and (Δ) meso-SAPO(C_{22-4-4} , 100). The pore size distribution was calculated via BJH algorithm using the adsorption branch.

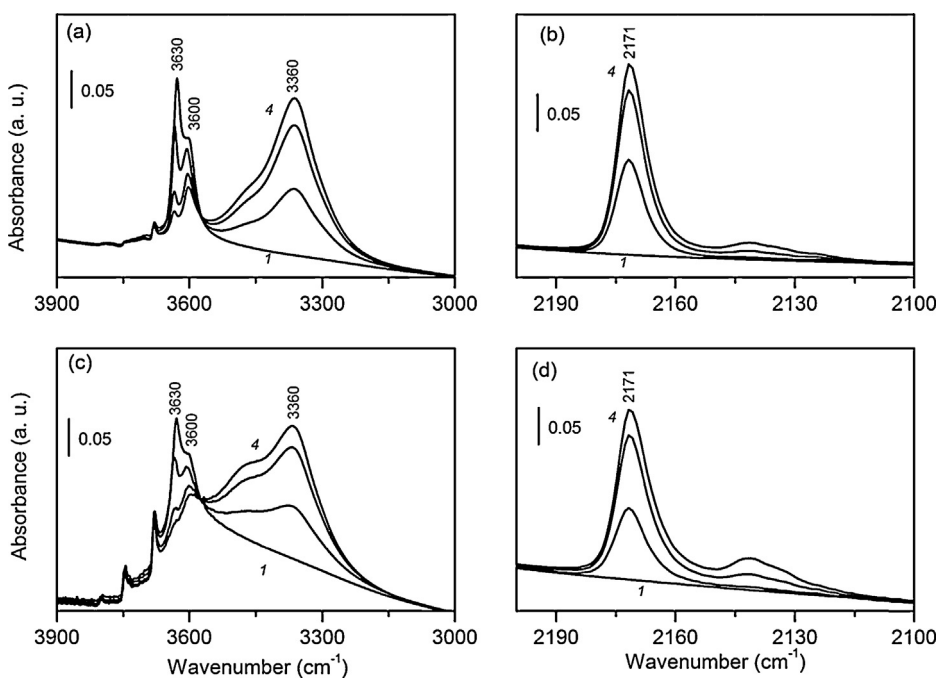


Fig. 7. FTIR spectra of CO adsorbed on SAPO-34 (a and b) and meso-SAPO(TPOAC, 0.04) (c and d) at liquid N₂ temperature: (left) OH stretching region, and (right) CO stretching region (trace 1 is the spectrum of dehydrated zeolite before CO adsorption; traces 2–4 after introduction of 0.55, 0.85, 1.20, 1.85 μmol CO in the IR cell; the spectra normalized by sample weight).

3.2. Catalytic activity measurements

We first discuss the performance of silylated mesoporous SSZ-13 in the MTO reaction. The rationale of silylating the most promising mesoporous SSZ-13 zeolite, meso-SSZ-13(C₂₂₋₄₋₄, 0.17) with a Si/Al ratio of 20 [8,9] was to evaluate whether deactivation of acid sites at or close to the external surface would have a beneficial effect on catalyst stability. Treatment of meso-SSZ-13(C₂₂₋₄₋₄, 0.17) with TEOS did not significantly affect the crystallinity of the mesoporous SSZ-13 zeolite (Fig. 8a), yet it lowered the silanol density. Fig. 8b shows the performance in the MTO reaction with reaction time. Clearly, the rate of coke formation was decreased. The product distributions (mainly C₂ and C₃ olefins) for both zeolites were similar (Table 2). These results indicate that there is room for improvement of the total methanol conversion capacity

of mesoporous SSZ-13 by lowering the rate of coke formation on or close to the external surface.

The catalytic activities of the SSZ-13 zeolites with a Si/Al ratio of 50 at a WHSV of 0.8 g g⁻¹ h⁻¹ are shown in Fig. 9 and the corresponding performance data are listed in Table 2. Initially, all catalysts show complete conversion of methanol to products with carbon–carbon bonds. For SSZ-13(50), the lifetime in MTO reaction is about 7 h, which is significantly higher than that of SSZ-13(20) (2.8 h) [8,9]. This shows that a lower Brønsted acid site density results in a lower rate of deactivation. When additional mesoporosity is introduced in SSZ-13(50) by use of TPOAC (meso-SSZ-13(50, TPOAC)), the lifetime of the catalyst is further improved. The increase in lifetime upon mesopore introduction in SSZ-13(50) is however much lower than earlier found for SSZ-13(20) [8,9]. This should be due to the lower rate of coke formation of SSZ-13(50),

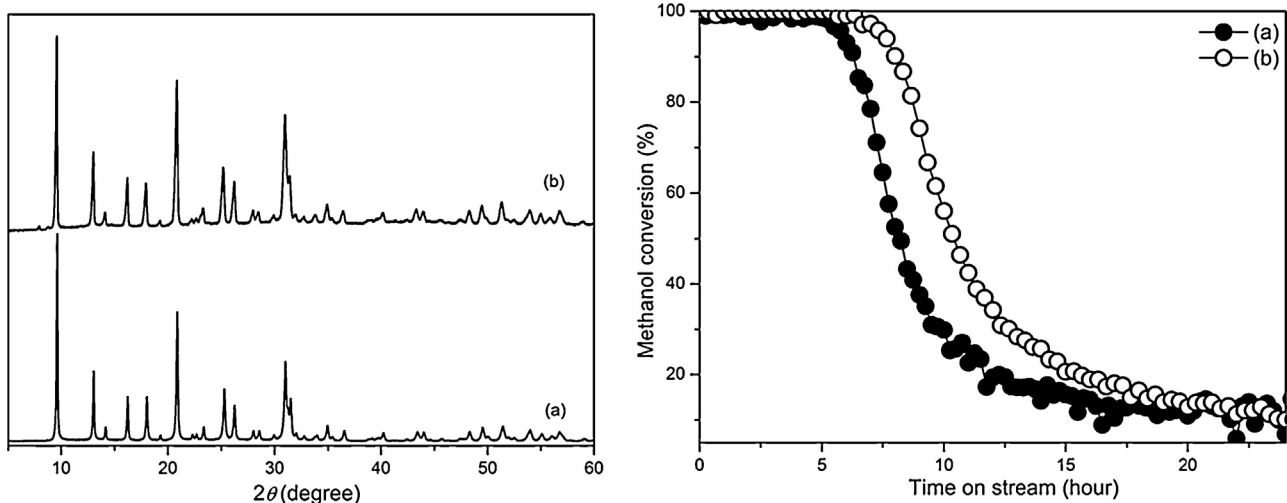


Fig. 8. (left) XRD patterns and (right) catalytic performance in the MTO reaction (WHSV = 0.8 g g⁻¹ h⁻¹; T = 350 °C) of calcined (a) meso-SSZ-13(C₂₂₋₄₋₄, 0.17) and (b) meso-SSZ-13(C₂₂₋₄₋₄, 0.17)-sil.

Table 2

Lifetime and product distribution^a of zeolite catalysts for the MTO reaction ($\text{WHSV} = 0.8 \text{ g g}^{-1} \text{ h}^{-1}$; $T = 350^\circ\text{C}$) after 1 h time on stream.

Zeolite	t_{50}^b (h)	CH_4 (%)	$\text{C}_2^=$ (%)	C_2 (%)	$\text{C}_3^=$ (%)	C_3 (%)	Aliphatic $\text{C}_4\text{--C}_6$ (%)
SSZ-13(50)	7	1.4	52.6	0.2	41.5	2.7	1.5
Meso-Zeo(50, TPOAC)	9	1.2	51.4	0.2	44.1	1.6	1.4
Meso-Zeo(C_{22-4-4} , 0.17) ^c	8	1.0	45.8	0.4	47.7	2.9	2.2
Meso-Zeo(C_{22-4-4} , 0.17)-sil	10	1.3	48.5	0.3	45.7	2.9	1.3

^a Trace amounts of CO and CO_2 not taken into account.

^b Catalyst lifetime defined as the time passed to reach a conversion of 50%.

^c [8].

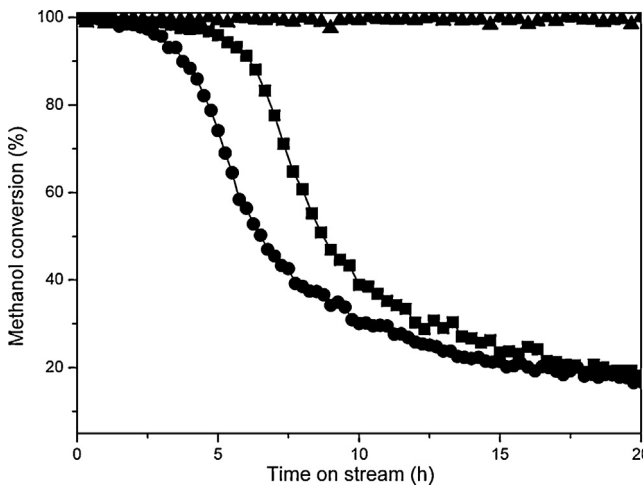


Fig. 9. Catalytic performance in the MTO reaction ($\text{WHSV} = 0.8 \text{ g g}^{-1} \text{ h}^{-1}$; $T = 350^\circ\text{C}$) of (●) SSZ-13(50), (▲) meso-Zeo(50, C_{22-4-4}) and (■) meso-Zeo(50, TPOAC).

which results in better utilization of the micropore space. The most stable zeolite is meso-Zeo(50, C_{22-4-4}), which had the MFI topology. This zeolite showed high stability in the methanol conversion reaction. As we were primarily interested in CHA zeolite in this study, we did not determine the stability of the ZSM-5 zeolite in further detail.

Fig. 10 shows the catalytic properties of the SAPO materials in the MTO reaction. The lifetime and the product distribution are given in Table 3. Meso-SAPO(TPOAC, ∞) shows some activity with a product distribution typical for ZSM-5 zeolite. The methanol conversion for meso-SAPO(C_{22-4-4} , 50) and meso-SAPO(C_{22-4-4} , 100) is very low. Both microporous SAPO-34 and meso-SAPO(TPOAC, 0.04) initially show complete conversion of methanol with good selectivity to C_2 and C_3 olefins. Deactivation of the mesoporous SAPO-34 zeolite sets in earlier than for the conventional SAPO-34 one. The lifetimes of SAPO-34 and meso-SAPO(TPOAC, 0.04) are 3 and 1.5 h, respectively. Thus, whilst the performance of SSZ-13 can be improved by introducing mesoporosity, such improvement could not be brought about for SAPO-34. It is well known that the Brønsted acid sites in SAPO-34 are much weaker than those in SSZ-13 [22,23]. Accordingly, it is expected that coking in SSZ-13 proceeds at a higher rate than in SAPO-34. The lower rate of coke formation for SAPO-34 may thus lead to more efficient utilization of the micropore space. As a consequence, there is no benefit by

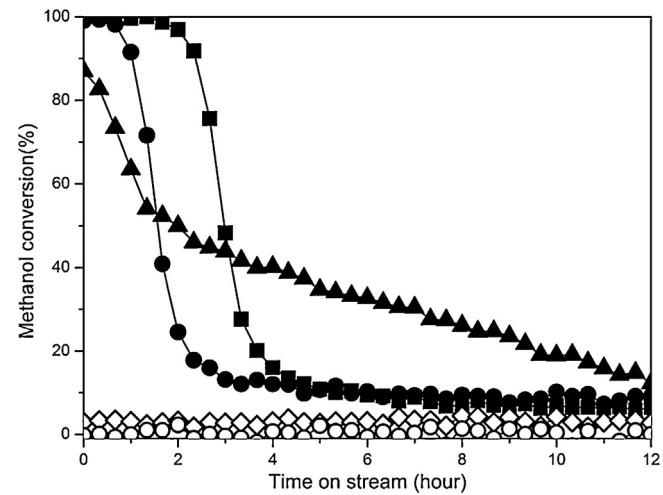


Fig. 10. Catalytic performance in the MTO reaction ($\text{WHSV} = 0.8 \text{ g g}^{-1} \text{ h}^{-1}$; $T = 450^\circ\text{C}$) of (■) SAPO-34, (●) meso-SAPO(TPOAC, 0.04), (▲) meso-SAPO(TPOAC, ∞), (◊) meso-SAPO(C_{22-4-4} , 50) and (○) meso-SAPO(C_{22-4-4} , 100).

generating mesoporosity in SAPO-34. If this would be the case, the lower stability of mesoporous SAPO-34 should be due to the lower concentration of Brønsted acid sites. A rough estimation based on the difference in the intensity of the CO stretching band around 2171 cm^{-1} shows that meso-SAPO(TPOAC, 0.04) contains about 40% less acid sites than SAPO-34. This difference coheres very well with the shorter lifetime, so that the total methanol conversion capacity of the two zeolites per Brønsted acid site is comparable. To fortify this line of reasoning, Table 4 shows the textural properties and coke content of SAPO-34 and meso-SAPO(TPOAC, 0.04) as the function of the time on the stream. After a reaction time of 1 h, already a large part of the high Langmuir surface area of the parent samples ($>700 \text{ m}^2 \text{ g}^{-1}$) has become inaccessible by coke. It is also seen that the micropore volume has decreased below $0.10 \text{ cm}^3 \text{ g}^{-1}$ (initial value $\sim 0.21 \text{ cm}^3 \text{ g}^{-1}$). With increasing time on stream the surface area of the two materials decreases in a very similar manner. The coke build-up is slightly slower for meso-SAPO(TPOAC, 0.04), which may be attributed to the lower acidity of this sample. Yang et al. recently reported that nanosizing SAPO-34 crystals led to a decrease in coke formation and, concomitant remarkable increase of the lifetime in the MTO reaction [25]. This discrepancy may be caused by the higher Brønsted acid intensity and the larger particle

Table 3

Lifetime and product distribution^a of SAPO-34 and meso-SAPO(TPOAC, 0.04) zeolite catalysts for the MTO reaction ($\text{WHSV} = 0.8 \text{ g g}^{-1} \text{ h}^{-1}$; $T = 450^\circ\text{C}$) after 1 h time on stream.

Zeolite	Lifetime ^b (h)	CH_4 (%)	$\text{C}_2^=$ (%)	C_2 (%)	$\text{C}_3^=$ (%)	C_3 (%)	Aliphatic $\text{C}_4\text{--C}_6$ (%)
SAPO-34	3.0	2.1	41.9	0.2	39.5	0	16.3
meso-SAPO(TPOAC, 0.04)	1.5	3.8	40.7	0.2	37.9	0	17.4
meso-SAPO(TPOAC, ∞)	2.0	4.5	16.1	0.2	34.9	0.5	43.8

^a Trace amounts of CO and CO_2 not taken into account.

^b Catalyst lifetime defined as the time passed to reach a conversion of 50%.

Table 4

Textural properties of spent SAPO-34 and meso-SAPO(TPOAC, 0.04) catalysts as a function of the time on stream determined by Ar physisorption.

TOS ^a (h)	SAPO-34				Meso-SAPO(TPOAC, 0.04)			
	S _L (m ² g ⁻¹)	V _{micro} (cm ³ g ⁻¹)	V _{meso} (cm ³ g ⁻¹)	Coke ^b (wt.%)	S _L (m ² g ⁻¹)	V _{micro} (cm ³ g ⁻¹)	V _{meso} (cm ³ g ⁻¹)	Coke ^b (wt.%)
1	347	0.09	0.08	3.5	300	0.08	0.09	3.6
4	295	0.07	0.10	11.7	284	0.07	0.11	6.9
12	164	0.04	0.07	12.8	191	0.05	0.08	8.0
48	149	0.04	0.06	13.7	141	0.07	0.10	10.0

^a Time on stream.

^b Coke content based on TGA.

size of their reference sample, and the much higher space velocity of the MTO reaction employed by these authors.

4. Conclusion

Several approaches to improve the catalytic performance of SSZ-13 and SAPO-34 for application as acid catalysts in the methanol-to-olefins (MTO) reaction were explored. Silylation of a mesoporous SSZ-13 zeolite with a Si/Al ratio resulted in minor improvement of the lifetime in the MTO reaction. Lowering the Al content of SSZ-13 to a Si/Al ratio of 50 resulted in lower rate of deactivation compared to SSZ-13 with a Si/Al ratio of 20 due to the lower density of Brønsted acid sites. Additional mesoporosity in SSZ-13(50) by use of an organosilane mesoporogen only results in a minor improvement of the lifetime. This is because the lower rate of coke formation for SSZ-13(50) as compared to SSZ-13(20) results in better utilization of the micropore space. It was not possible to synthesize mesoporous SSZ-13 at high Si/Al ratios with the C₂₂-4-Br₂ template. Instead, ZSM-5 zeolite was obtained.

Attempts to synthesize SAPO-34 by use of C₂₂-4-Br₂ as mesoporogen were also not successful and other AlPO phases were obtained. By use of TPOAC a mesoporous SAPO-34 was obtained. The intracrystalline mesoporosity did not lower the deactivation rate. The total methanol conversion capacity per acid site for microporous and mesoporous SAPO-34 was comparable. These findings are interpreted in terms of complete utilization of the micropore of SAPO-34 in the MTO reaction. The very different findings for SSZ-13, whose micropore space remains underutilized unless mesopores are introduced, relate to the much lower acidity of silicoaluminophosphates. Accordingly, there is no benefit of additional mesoporosity for SAPO-34.

Acknowledgments

Financial support from the Technology Foundation STW, the applied science division of The Netherlands Organization for Scientific Research (NWO) and the Programme Strategic Alliances between China and the Netherlands is acknowledged. We also thank the Soft Matter Cryo-TEM Research Unit of Eindhoven

University of Technology and the SACHEM company for providing N,N,N-trimethyl-1-adamantanammonium hydroxide.

References

- [1] C.D. Chang, Catal. Rev. Sci. Eng. 26 (1984) 323–345.
- [2] M. Stocker, Microporous Mesoporous Mater. 29 (1999) 3–48.
- [3] J.F. Haw, W.G. Song, D.M. Marcus, J.B. Nicholas, Acc. Chem. Res. 36 (2003) 317–326.
- [4] F.J. Keil, Microporous Mesoporous Mater. 29 (1999) 49–66.
- [5] U. Olsbye, S. Svelle, M. Bjørgen, P. Beato, T.V.W. Janssens, F. Joensen, S. Bordiga, K.P. Lillerud, Angew. Chem. Int. Ed. 51 (2012) 5810–5831.
- [6] J. Liang, H.Y. Li, S. Zhao, W.G. Guo, R.H. Wang, M.L. Ying, Appl. Catal. 64 (1990) 31–40.
- [7] Z.M. Liu, C.L. Sun, G.W. Wang, Q.X. Wang, G.Y. Cai, Fuel Process. Technol. 62 (2000) 161–172.
- [8] L. Wu, V. Degirmenci, P.C.M.M. Magusin, N.J.H.G.M. Lousberg, E.J.M. Hensen, J. Catal. 298 (2013) 27–40.
- [9] L. Wu, V. Degirmenci, P. Magusin, B.M. Szija, E.J.M. Hensen, Chem. Commun. 48 (2012) 9492–9494.
- [10] M. Choi, H.S. Cho, R. Srivastava, C. Venkatesan, D.H. Choi, R. Ryoo, Nat. Mater. 5 (2006) 718–723.
- [11] M. Choi, K. Na, J. Kim, Y. Sakamoto, O. Terasaki, R. Ryoo, Nature 461 (2009) 246–250.
- [12] M. Choi, R. Srivastava, R. Ryoo, Chem. Commun. (2006) 4380–4382.
- [13] C. Jo, J. Jung, H.S. Shin, J. Kim, R. Ryoo, Angew. Chem. Int. Ed. 52 (2013) 10014–10017.
- [14] S.M.T. Almutairi, B. Mezari, E.A. Pidko, P.C.M.M. Magusin, E.J.M. Hensen, J. Catal. 307 (2013) 194–203.
- [15] M. Guisnet, L. Costa, F.R. Ribeiro, J. Mol. Catal. A: Chem. 305 (2009) 69–83.
- [16] Y. Kumita, J. Gascon, E. Stavitski, J.A. Moulijn, F. Kapteijn, Appl. Catal., A: Gen. 391 (2011) 234–243.
- [17] L.T. Yuen, S.I. Zone, Verified Syntheses of Zeolitic Materials, in: H. Robson (Ed.), Synthesis Commission of the International Zeolite Association, 2nd ed., Elsevier, 2001.
- [18] S.R. Zheng, H.R. Heydenrych, A. Jentys, J.A. Lercher, J. Phys. Chem. B 106 (2002) 9552–9558.
- [19] B.M. Lok, C.A. Messina, R.L. Patton, R.T. Gajek, T.R. Cannon, E.M. Flanigen, U.S. Patent 4440871, 1984.
- [20] J.J. Pluth, J.V. Smith, J.M. Bennett, J.P. Cohen, Acta Crystallogr. Sect. C: Cryst. Struct. Commun. 40 (1984) 2008–2011.
- [21] J.B. Parise, Acta Crystallogr. Sect. C: Cryst. Struct. Commun. (1984) 1641–1643.
- [22] S. Bordiga, L. Regli, D. Cocina, C. Lamberti, M. Bjørgen, K.P. Lillerud, J. Phys. Chem. B 109 (2005) 2779–2784.
- [23] F. Bleken, M. Bjørgen, L. Palumbo, S. Bordiga, S. Svelle, K.P. Lillerud, U. Olsbye, Top. Catal. 52 (2009) 218–228.
- [24] S.M.T. Almutairi, B. Mezari, G.A. Filonenko, P. Magusin, M.S. Rigutto, E.A. Pidko, E.J.M. Hensen, ChemCatChem 5 (2013) 452–466.
- [25] G. Yang, Y. Wei, S. Xu, J. Chen, J. Li, Z. Liu, J. Yu, R. Xu, J. Phys. Chem. C 117 (2013) 8214–8222.